Research Article Vol. 30, No. 14 / 4 Jul 2022 / Optics Express 25177
Optics EXPRESS

Rigorous dynamic model of a silicon ring resonator with phase change material for a neuromorphic node

ALESSIO LUGNAN,[1,*] SANTIAGO GARCÍA-CUEVAS CARRILLO,[2] C. DAVID WRIGHT,[2] AND PETER BIENSTMAN[1]

[1] *Ghent University/imec, Gent, Belgium*
[2] *Department of Engineering, University of Exeter, Exeter, UK*
[*] *alessio.lugnan@ugent.be*

Abstract: The photonics platform has been considered increasingly promising for neuromorphic computing, due to its potential in providing low latency and energy efficient large-scale parallel connectivity. Phase change materials (PCMs) have been recently employed to introduce all-optical non-volatile memory in integrated photonic circuits, especially finding application as non-volatile weighting element in photonic artificial neural networks. Interestingly, these weighting elements can potentially be used as building blocks for large-scale networks that can autonomously adapt to their input, i.e. presenting the property of *plasticity*, similarly to the biological brain. In this work, we develop a computationally efficient dynamical model of a silicon ring resonator (RR) enhanced by a phase change material, namely $Ge_2Sb_2Te_5$ (GST). We do so starting from two existing dynamical models (of a silicon RR and of a GST thin film on a straight silicon waveguide), but extending the optical equations to properly account for the high absorption and asymmetry in the ring due to the phase change material. Our model accounts for silicon nonlinear effects due to free carriers and temperature, as well as for the phase change of GST, whose energy efficiency and optical contrast can be enhanced by the RR resonant behaviour. We also restructure the optical equations so that the model can be efficiently employed in a modular way within a commercial software for system-level photonics simulations. Moreover, exploiting the developed model, we explore several design parameters and show that both speed and energy efficiency of memory operations can be enhanced by factors from six to ten. Also, we show that the achievable optical contrast due to GST phase change can be increased by more than a factor ten by leveraging the resonant properties of the RR, at the expense of higher optical loss. Finally, by exploiting the nonlinear dynamics arising in silicon RR networks, we show that a strong contrast is achievable while preserving energy efficiency.

1. Introduction

Photonics is a promising platform for scaling up neuromorphic computing in a sustainable way, as it can significantly outperform electronics in energy efficiency and parallelism of communication, enabling the large-scale connectivity required by hardware implementations of *artificial neural networks* (NNs) at low energy cost and latency [1]. However, training hardware neuromorphic systems still poses several important challenges [2–4]. One major reason is that *backpropagation*, i.e. the method of choice to train software-based NNs, generally requires accurate control over the network parameters, knowledge of the loss function gradient w.r.t. parameters and full observability of the system's internal states. These requirements significantly limit the scalability of physical networks. In contrast, the human brain learns by letting its network parameters adapt (e.g. through *synaptic plasticity*) to the propagating signals that carry information through the biological neural network, achieving far superior performance despite consuming only the power of two LED light bulbs [5]. In other words, the response of the components of the brain

#459364 https://doi.org/10.1364/OE.459364
Journal © 2022 Received 25 Mar 2022; revised 10 Jun 2022; accepted 12 Jun 2022; published 27 Jun 2022

Optics EXPRESS

depends on their past input, i.e. they exhibit *non-volatile memory*, or *plasticity*, w.r.t. their input signal. Inspired by the brain, a lively research interest has grown towards developing effective *biologically plausible* training algorithms, often based on plastic properties of network nodes or connections [6–8].

Recently, non-volatile all-optical memory based on *phase change materials* (PCMs), using $Ge_2Sb_2Te_5$ (GST for short) in particular, was introduced into integrated photonic circuits [9,10], bringing a convenient source of plasticity into play. In particular, GST-based devices were employed for arithmetic operations [11,12] and as neuro-synaptic components to build or accelerate NNs [13–17]. GST presents a strong complex refractive index contrast between its amorphous and crystalline phase. Moreover, the phase of a thin GST layer deposited on top of a waveguide can be changed by optical input pulses of appropriate powers and lengths, so that many different levels of waveguide transmission can be obtained. These memory operations are relatively fast (down to tens of ns) and can be reversed many times [18]. The photonic platform of choice is usually silicon nitride, which presents overall higher efficiency and memory operation contrast than silicon, due to the lower optical mode confinement and thermal dissipation [19]. Nonetheless, the silicon photonics platform has an advantage in terms of integration, device footprint and speed of memory operations [19].

In order to build scalable plastic neuromorphic photonic systems, *cascadability* of memory and nonlinear operations is key. In this context, cascadability is the degree to which an input signal (one or more optical spikes) is able to activate the nonlinear and plastic behaviour of a large number of network components connected in series, in a way that the activation of each device is dependent on the activation of the previous ones in the series. However, the plastic devices based on conventional rib-type straight waveguides with integrated GST cells on top tend to require relatively powerful optical pulses to change the memory state, and present quite high optical loss, especially when the GST is in the crystalline phase and the silicon photonics platform is considered. This significantly limits cascadability of these devices when employed as components in a photonic NN.

In this work we investigate and propose to exploit the combination of optical resonance and low-power nonlinear effects in silicon *ring resonators* (RR) [20], in order to build more cascadable plastic nodes for scalable photonic networks. In particular, the optical response of a RR presents an increased sensitivity to small variations in complex refractive index of its internal ring waveguide. Therefore, by covering a shorter length of the ring waveguide with GST, it is still possible to obtain high contrast due to phase change. This improves energy efficiency of memory operations in two ways: first, the phase state of a shorter GST cell obviously requires less optical energy to be modified; second, lower cavity losses due to a shorter GST cell allow the RR to accumulate more optical energy when resonant (higher cavity finesse), enhancing the internal power w.r.t. the input power. Such a power enhancement allows us to change the GST material phase distribution using a lower input optical power. These improvements can, for example, compensate for the disadvantages of the silicon photonics platform w.r.t. to the silicon nitride platform, i.e. lower energy efficiency and lower contrast of memory operations [19].

It should be stressed that there are several other experimental or simulation-based published works that focus on RRs partially coated with GST [9,14–16,21–26]. However, to the best of our knowledge, none of those considered to exploit the enhanced power and sensitivity of the ring waveguide to improve energy efficiency and optical contrast of GST phase change. Moreover, the models and simulations employed in the other works did not fully account for the dynamics of silicon nonlinear effects. In fact, the enhanced power level in the silicon ring waveguide can easily trigger competing nonlinear effects, due to an increase of free carrier density (with faster timescale, around 5 ns) and temperature (with slower timescale, around 100 ns). These effects can temporarily but significantly modify the RR resonance wavelength and thus the effective

Optics EXPRESS

coupling strength with the input-output waveguides. Therefore, it is important to consider these effects when simulating or designing plastic optical devices based on a silicon RR with GST.

Nonetheless, the aforementioned nonlinear effects can be exploited, in combination with the non-volatile memory given by GST, to implement scalable neuromorphic computing systems within a small footprint. In particular, these effects can provide the nonlinear activation function required by neurons, together with short-term and long-term nonvolatile memory, which can greatly expand the network's effective temporal dimension without any footprint increase. In addition, RRs present a spectrum with many quasi-periodic resonances that are all linked together by silicon nonlinear effects and the GST crystalline fraction, providing an additional dimension for effective network expansion, i.e. through wavelength division multiplexing approaches. Finally, considering several silicon RRs with GST connected in series and with aligned resonance wavelengths, a pulse used to modify the memory state of the first RR might also have the effect of temporarily shifting its resonance away from the laser wavelength, freeing the way for a second laser pulse, which can reach the second device undisturbed, and so on. Such a mechanism has the potential to make these plastic devices very cascadable in practice, if design parameters are suitably chosen.

In this article, we first derive a computationally efficient numerical model that accounts for both the GST unit cell dynamical behavior (by integrating the compact behavioural model proposed in [26]) and the main silicon nonlinear effects in the RR, for the first time. In contrast to previous models, we accurately model the asymmetry introduced by the GST cell and we write optical equations based on the time-dependent couple mode theory (CMT) without the usual high finesse approximations. To motivate and validate these modifications, we show that they significantly improve the accuracy of the RR steady-state response for different example cases. Then we mathematically restructure the model so that it can be efficiently employed in a modular way for system-level simulations, within a commercial circuit simulator for photonic integrated circuit design (*Luceda Caphe*). In the second part, we employ the derived model to show that a silicon RR with a short GST cell is a particularly promising neuromorphic element in terms of speed and efficiency of memory operations. Moreover, we show that the GST crystalline fraction can have a strong impact (high contrast both in terms of output optical power and phase) on the nonlinear dynamics arising in a small silicon RR network. These results show that the proposed devices are promising candidates as all-optical plastic nodes with high cascadability for dynamical neuromorphic systems, such as photonic recurrent NNs.

2. Model development

In this section we describe the development of a numerical model for integrated silicon RRs with a PCM cell (namely a GST layer on top of part of the ring waveguide), which can be used to efficiently simulate this component both in time and frequency domain, as a building block of photonic integrated circuits. The model is implemented and evaluated using a commercial photonic integrated circuit (PIC) simulator (*Luceda Caphe*).

2.1. Time-dependent coupled mode theory (TCMT) model of a silicon RR

2.1.1. Mathematical structure of a Caphe TCMT model

In this work we build on an existing node-based simulator for large-scale photonic circuits that works both in frequency and time domain [27]. It allows for fast circuit analysis through a high-level simplified description of the optical signal propagation, similarly as in *coupled mode theory* [28] (CMT). In particular, time-domain simulations are sped up by virtually splitting a circuit in *memory-containing* (MC) components and *memoryless* (ML) components, the latter not requiring costly time-dependent simulations. In practice, we employ a commercial

Optics EXPRESS

implementation of such simulator, which is called *Caphe* and is part of *Luceda*'s environment for PIC design.

In this work, we are interested in time-domain simulations of microring resonators excited with monochromatic infrared light (wavelengths around 1550 nm), where the relevant nonlinear effects of silicon and of the GST layer can be accounted for. *Caphe* employs a specific mathematical structure for these kinds of nonlinear optical cavities, called *TCMT models*, which is based on the *time-dependent CMT* formalism (see [29] or section 3.9 of [30]). A TCMT model is shaped so that it builds a circuit node with an arbitrary number of input ports, output ports and internal variables whose time evolution is described through coupled $1st$ order ordinary differential equations (ODEs).

In particular, let us consider a time-dependent vector $\boldsymbol{v}(t)$, whose elements are the internal variables of a TCMT model, and a vector $\boldsymbol{s}_{\text{in}}(t)$, whose elements are given input signals. The time evolution of $\boldsymbol{v}(t)$ is governed by the following 1^{st} order ODE in its general form:

$$\frac{d}{dt}\boldsymbol{v}(t) = \boldsymbol{M}\boldsymbol{v}(t) + \boldsymbol{K}^{\boldsymbol{T}}\boldsymbol{s}_{\text{in}}(t) + \boldsymbol{N}(\boldsymbol{v}(t), t) \tag{1}$$

where $\boldsymbol{M}$ and $\boldsymbol{K}^{\boldsymbol{T}}$ are complex-valued constant matrices, and $\boldsymbol{N}$ is a complex-valued vector function that can be time-dependent. Specifically, the linear contribution of $\boldsymbol{v}$ to its own time derivative is expressed by $\boldsymbol{M}$, while the nonlinear contributions are expressed by the function $\boldsymbol{N}$. Note that $\frac{d}{dt}\boldsymbol{v}$ depends only linearly on the input signals in $\boldsymbol{s}_{\text{in}}$. The output signals, collected in the vector $\boldsymbol{s}_{\text{out}}(t)$, are given in general by a linear combination of the inputs and the internal variables:

$$\boldsymbol{s}_{\text{out}}(t) = \boldsymbol{S}\boldsymbol{s}_{\text{in}}(t) + \boldsymbol{D}\boldsymbol{v}(t) \tag{2}$$

where $\boldsymbol{S}$ and $\boldsymbol{D}$ are suitable complex-valued constant matrices. The restrictions imposed by this mathematical structure allow for faster simulations of circuits comprising several TCMT nodes both in time and frequency domain.

2.1.2. Dynamical model of a high finesse silicon RR

A TCMT model for time-domain simulations of a high finesse silicon RR is described in [31], where an *all-pass* configuration (i.e. with one coupled waveguide, see Fig. 1) is excited by infrared monochromatic light. In the next sections we will expand this model to take into account the asymmetry introduced by the GST cell, but before doing that, we describe the original basic model here in this subsection, going only into the details that are most important for our case. The model accounts for the most relevant nonlinear dynamics in a silicon RR, which arise from the coupling between optical power, temperature and free carrier concentration in the silicon ring waveguide. In particular, the physics behind the considered nonlinear effects can be summarized as follows.

The two photon absorption (TPA) effect, which is responsible for an increase in silicon optical absorption proportional to the square of the optical power, generates free carriers. These populate the ring waveguide for a certain time, before they recombine or diffuse away. The presence of free carriers increases both light absorption, through the free carrier absorption (FCA) mechanism, and the silicon refractive index, due to the free carrier dispersion (FCD) effect, resulting in a blueshift of the RR resonance wavelength. The total absorbed electromagnetic power heats up the waveguide, so that the silicon refractive index is increased through the thermo-optic effect (TOE) and the RR resonance is redshifted.

Interestingly, FCD and TOE are responsible for opposite shifts in resonance wavelength. Moreover, the first effect is typically weaker but significantly faster than the second one (example characteristic times are 5.3 ns and 65 ns respectively). Under these conditions, a silicon RR excited with a strong enough and constant optical signal can exhibit a periodic oscillation of its resonance wavelength, emitting a pulsed optical signal at its output [31,32]. The dynamic

Optics EXPRESS

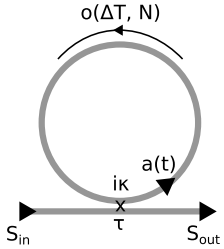

Fig. 1. A schematic of a RR in all-pass configuration (i.e. with one coupled waveguide): s_{in} and s_{out} represent the input and the output optical signals respectively; a is the mode amplitude of the optical signal travelling inside the ring; a straight waveguide is coupled to the ring waveguide through a directional coupler whose transmission and coupling coefficients are represented by τ and κ respectively; o is the complex factor accounting for the attenuation and the phase shift applied to $a(t)$ when travelling one ring round trip, not including the coupling transmission τ. For high enough input powers, o significantly depends on the excess ring temperature ΔT and on the amount of free carriers N.

CMT description under consideration is mainly built to account for this phenomenon, called *self-pulsing*.

Now, let us see how Eq. (1) is applied to the all-pass RR case we just described, considering a single-mode ring waveguide, input light with wavelength λ that is close to a given resonance wavelength λ_r and neglecting backscattering. The internal variables contained in the vector $\boldsymbol{v}(t)$ are:

1. $a(t)$, the complex amplitude of the RR optical mode, in the context of the *slowly varying envelope approximation*, normalized so that its squared modulus equals the electromagnetic energy in the ring at time t.
2. $\Delta T(t)$, the mode-averaged temperature difference w.r.t. the environment.
3. $N(t)$, the number of free carriers populating the RR.

The employed system of equations, written as an element-wise splitting of Eq. (1), is [31–33]:

$$\frac{d}{dt}a = \left[i(\omega_r + \delta\omega_r(\Delta T, N) - \omega) - \mathcal{L}_l - \mathcal{L}_{\text{nl}}(|a|^2, N)\right] a + \frac{i\kappa}{\sqrt{T_r}} s_{\text{in}}(t) \tag{3}$$

$$\frac{d}{dt}\Delta T = -\frac{\Delta T}{\tau_{\text{th}}} + \mathcal{A}_{\text{th}}(|a|^2, N) \tag{4}$$

$$\frac{d}{dt}N = -\frac{N}{\tau_{\text{fc}}} + \mathcal{A}_{\text{fc}}(|a|^2) \tag{5}$$

In the first ODE (Eq. (3)), the term $i(\omega_r + \delta\omega_r(\Delta T, N) - \omega)$ represents the influence of the detuning between the light source angular frequency ω and the resonance angular frequency $\omega_r + \delta\omega_r(\Delta T, N)$ of the RR, where ω_r is its unperturbed value and $\delta\omega_r$ a time-dependent perturbation. The terms $\mathcal{L}_l$ and $\mathcal{L}_{\text{nl}}(|a|^2, N)$ respectively provide the damping effect of the linear (unperturbed) and the nonlinear cavity losses. The coupling factor $i\kappa/\sqrt{T_r}$ determines the ring excitation by the input optical signal $s_{\text{in}}(t)$, which is a mode complex amplitude similarly as $a(t)$, but with the difference that it is normalized so that $|s_{\text{in}}(t)|^2$ equals the input power at time t. In particular, $i\kappa$ is the coupling coefficient of the directional coupler and $T_r = L/v_g$, where L and v_g are respectively the length and the group velocity of the ring waveguide. T_r is called the *round trip time* and approximately estimates the time needed by an optical signal to travel one

Optics EXPRESS

round trip through the ring. Since approximately all the energy $|a|^2$ stored in the ring has to pass through a given ring cross section in a round trip time T_r, we set $|s_{\text{ring}}|^2 = |a|^2/T_r$, where $|s_{\text{ring}}|^2$ is the optical power flowing in the ring and s_{ring} is the corresponding mode complex amplitude. Therefore $\sqrt{T_r}$ is in this case a factor that translates power mode amplitudes, such as s_{in} and s_{out}, into energy mode amplitudes, such as a. In the last two ODEs , τ_{th} and τ_{fc} are the relaxation times for respectively ΔT and N, while $\mathcal{A}_{\text{th}}$ and $\mathcal{A}_{\text{fc}}$ respectively represent their source, given by the absorption of the signal a in the ring waveguide. A derivation of Eq. (3) is discussed in the Supplement 1 (Section 1). Additionally, further details and the full derivation of these equations can be found in [32] and in [30].

Finally, the equation for the output signal is:

$$s_{\text{out}}(t) = \tau s_{\text{in}}(t) + \frac{i\kappa}{\sqrt{T_r}} a(t) \tag{6}$$

This corresponds to the optical mixing performed by the directional coupler, where $\tau = \sqrt{1-\kappa^2}$ is its transmission coefficient and $a(t)/\sqrt{T_r}$ is the power amplitude in the ring waveguide. (Note that strictly speaking, this equation is only valid for the exact model, and not for the approximate model where κ is taken to be small, in which case τ should be 1 for consistency reasons.)

It should be stressed that the nonlinear perturbations in the ODEs, as well as ΔT and N, are negligible for a low enough optical input power $|s_{\text{in}}(t)|^2$, typically $\ll 1$ mW. Moreover, the first ODE (Eq. (3)) is valid for high-finesse RRs, i.e. for small ring losses and coupling coefficient ($\mathcal{L}_l \ll 1/T_r$ and $\kappa \ll 1$). Moreover, it should be noticed that a more accurate equation for the ODE governing the temperature was recently reported [34], which might allow for a more accurate fit of experimental data.

In the all-pass configuration that we considered until now, all the input optical power that is not transmitted through the output is lost through absorption and radiation loss. In this work, instead, we consider a RR coupled with two waveguides (*add-drop* configuration, see Fig. 2 (b)), since such a configuration is arguably more interesting for neuromorphic computing, where network connectivity and energy efficiency are key aspects. Indeed, the add-drop configuration allows for two input signals to interact in the ring and a single input can be split, depending on the resonance, among two output ports. This allows us, for example, to connect a few add-drop RRs to form optical networks that present very rich dynamics, such as chaotic behavior, and non-localized resonances coming from the interaction of two or more resonators [33,35]. These characteristics are especially interesting for hardware reservoir computing [36].

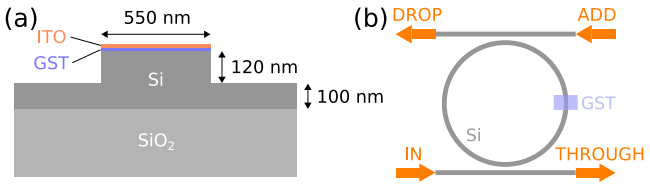

Fig. 2. (a): Cross section of the PCM cell, i.e. a rib silicon waveguide with PCM (GST) layer, modelled by the considered GST model [26]. The GST layer and the ITO protective layer are both 10 nm think. (b): Schematic of a silicon RR with GST cell, in the *add-drop* configuration (i.e. with two couples waveguides).

In Section 2.4 we will discuss the first ODE (Eq. (3)) in more detail and we will propose suitable modifications to account for the presence of a PCM layer on a segment of the ring waveguide.

Optics EXPRESS

2.2. Introduction of a compact behavioural model of GST cell in a dynamical RR model

In this work we aim to simulate the dynamical behaviour of a silicon RR when a small part of its waveguide is covered with a thin PCM layer [16,19] (GST in our case, see Fig. 2). We do so by combining two pre-existing numerical models: a dynamical model of a waveguide with a PCM cell and a dynamical RR model such as the one described in Section 2.1 (then adapted for our specific case in Section 2.4). In particular, we are interested in developing a modular model that can easily be used as building block in larger circuit simulations, comprising several photonic devices. For this purpose, we incorporated the compact behavioural model described in [26], whose parameters were suitably modified to simulate a silicon waveguide covered with a GST layer (see Section 4 in the Supplement 1 for details) and which will be referred to as the *GST model* from now on, into a RR TCMT simulator.

The pre-existing GST model allows to predict how a pump optical pulse (tens of nanoseconds long and with peak power from few to few tens of milliwatts) that excites the single-mode silicon waveguide may change the position of the amorphous-crystalline phase interface in the thin GST layer. In particular, the GST layer is modelled so that such interface can only move along one direction, i.e. parallel to the waveguide. Intuitively, if the interface is at the beginning (front edge) of the layer, the GST cell is completely crystalline and its strong light absorption implies a weak waveguide transmission. On the other hand, if the interface is located at the end (back edge) of the layer, the GST cell reached its maximum amorphization degree, corresponding to the maximum waveguide transmission. Intermediate phase interface positions provide intermediate waveguide transmissions. In the model, also the effective refractive index of the waveguide (and thus the phase shift of the propagated light) depends on the GST amorphous fraction, but the effect is weaker. However, as opposed to changes in absorption, the parameters regarding the changes in effective index were not directly validated through experiments in [26]. The dynamics of the phase interface are driven by the temperature of the GST layer, which in turn depends on the heating caused by the optical power propagating through the waveguide. In spite of its significant simplifications, the GST model can accurately fit experimental data (see [26] and Section 4 of the Supplement 1). In order to host the GST model and properly account for the additional physical properties, in Section 2.4 and in Section 3 of the Supplement 1 we developed a dedicated RR Caphe model by suitably modifying the pre-existing one. Essentially, in the resulting TCMT Caphe model we added two more ODEs to Eqs. (3), (4) and (5), governing the time evolution of the variables T_{GST} and z_{int} (these ODEs can be found in [26]). The first variable is the temperature of the GST layer while the latter is the position of the amorphous-crystalline phase interface in the GST layer. It should be stressed that, even if in [26] a model of a RR with GST is proposed, it does not account for silicon nonlinear effects and the related dynamics, as opposed to the TCMT model we develop in this work.

The main input and output quantities of the GST model are respectively the input optical power and the complex effective index of the waveguide covered with PCM. Therefore, keeping in mind the configuration we want to simulate (Fig. 2 (b)), the simplest way of combining this model with a RR model is to run the two models in parallel so that, at each timestep, the RR provides the input optical signal to the GST waveguide segment, which in turn updates its complex effective index. In this case, a change in complex effective index of the ring waveguide segment simply results in a variation of the attenuation and of the phase shift of the light passing through it, respectively resulting in a change of width and position of the RR resonance peak in the frequency domain.

Also note that the complex refractive index provided by the GST model depends both on the corresponding temperature at that location of the waveguide, and on the degree of amorphization of the GST layer.

Optics EXPRESS

2.3. Test comparison with numerical steady-state calculation

In Section 2.4 we will modify the optical equations of the TCMT model, i.e. Eq. (3) (or see Eq. (S6) in the Supplement 1 for a more detailed version of it) and Eq. (6), in order to account for the high losses and asymmetry due to the introduction of the GST cell. To motivate such modifications, but also to check the correctness of the employed differential equations and of the implemented code, we compare the linear steady-state response computed using the following three optical models (Fig. 3):

1. A naive model (called "uncorrected" in the shown plots) based on Eq. (S6) in the Supplement 1 and on Eq. (6), where the optical loss due to GST (comprising the scattering loss) is simply incorporated in the attenuation coefficient α of the ring waveguide (so that the factor $e^{-\alpha L}$ accounts for the the field amplitude attenuation due to both the ring waveguide and the GST cell).

2. Our proposed model (called "corrected" in the shown plots) based on Eqs. (11), (12) and (13), which are derived in Section 2.4.

3. A simple steady-state calculation (called "analytical" in the shown plots, see Section 5 of the Supplement 1 for details). Importantly, such a steady-state analysis accounts for the asymmetric addition of the GST cell and does not assume any approximation regarding time-domain behaviour or small resonance detuning. Moreover, it is based on simple analytical formulas and it does not require any numerical integration of differential equations.

The main parameters employed for this comparison, regrading the ring silicon waveguide, are: the effective index $n_{\text{eff}}Si = 2.7$, the group index $n_g^{Si} = 3.8$, the radius $R \approx 15\,\mu\text{m}$ and the attenuation coefficient $\alpha_{\text{Si, dB}} = 8\text{dB/cm}$. Regarding the ring waveguide segment covered by crystalline GST: the scattering loss $A^2_{\text{scat}} = 0.97$, length $L_{\text{GST}} = 0.5\,\mu\text{m}$ and complex effective index $n_{\text{eff,c}}GST = 2.69512 - i0.039111$ (see Section 4 of the Supplement 1). The power coupling of the ring to the waveguide is chosen to be $\kappa^2 = 0.15$. To obtain steady-state linear spectra from the developed dynamical RR model for the validation test, we run a short time-domain simulation for each input wavelength and at low input power (linear regime). As a first example, we simulated the excitation of the *in* port only and we considered a resonance with even azimuthal number $m = 164$ (Fig. 3(a)). In such a case, it can be noticed that the "uncorrected" model presents a significant error in its transmission spectrum w.r.t. the expected steady-state behaviour, which is given by the "analytical" model. However, the error in the corresponding phase shift spectrum is less pronounced. As a second example, the *in* and *add* ports were excited with the same phase and two constant optical power levels of ratio 2:1, while the same even azimuthal number was considered (Fig. 3 (b)). In this case, instead, the "uncorrected" model presents a substantial error also in its phase shift response. As a third and final example, we considered the same simulation with the only difference of employing an odd azimuthal number $m = 165$ (Fig. 3 (c)). In this case, since the two input beams with aligned phase interfere destructively in the ring waveguide, a very different response is obtained w.r.t. the even azimuthal number case. To account for this in the "uncorrected" model, we adjusted the equations by changing the sign of the terms connecting a with the *add* and the *drop* ports. Finally, we can notice that steady-state response of the proposed "corrected" model is in very good agreement with the expected "analytical" response in all cases. For completeness, in Section 6 of the Supplement 1 we also show plots corresponding to the ones in Fig. 3, with the only difference that the RR inputs are switched (the higher input power is at the *add* port and the lower at the *in* port). In the next section we will discuss the derivation of our "corrected" model and we will outline the differences w.r.t. the "uncorrected" model.

Optics EXPRESS

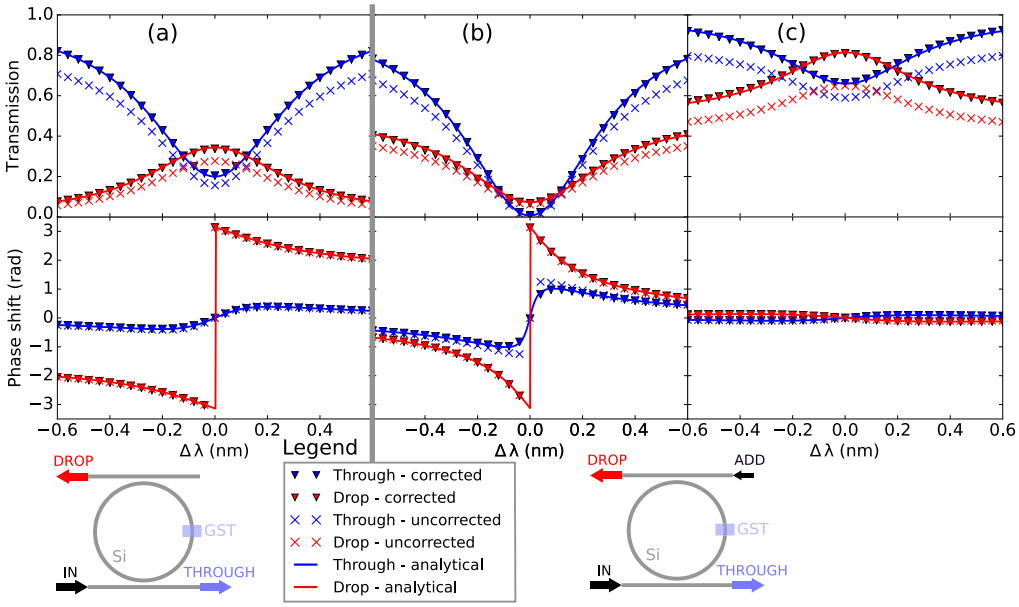

Fig. 3. Linear steady-state response (to a constant low-power input) of our "corrected" RR dynamical model with GST cell (discussed in Section 2.4) in comparison with an "uncorrected" naive implementation of the dynamical model (see Eq. (S6) in the Supplement 1) and with the expected "analytical" steady-state calculation (see Section 5 of the Supplement 1). The power coupling coefficients are set to 0.15 and the crystalline GST cell length to 0.5 μm. (a) Only the *in* input port is excited, as shown by the bottom left RR schematic. A resonance with even azimuthal number (namely 164) is considered. (b), (c) Respectively corresponding to an even and an odd azimuthal number (namely 164 and 165), the *in* and *add* input ports are excited with the same phase and two constant optical power levels of ratio 2:1, as shown by the bottom right schematic. In (c), the "uncorrected" model was adjusted to account for the sign changes due to an odd azimuthal number.

2.4. *Optical dynamical CMT equations for a silicon RR with PCM cell*

As we explained in Section 2.2, the considered PCM model, which accounts for the GST cell, provides the complex effective index of the corresponding waveguide segment, which depends on the solid state phase of the GST layer. In particular, the optical loss of the PCM cell is much higher than the loss in a corresponding silicon waveguide without GST, and it varies significantly when the GST phase distribution is changed. Namely, the absorption loss is estimated to be around 1.377 dB/μm and 1.152 dB/μm respectively for the maximum and the minimum achievable crystalline fraction (see Section 4 in the Supplement 1 for more details), while the scattering loss is estimated to be around 3%. Moreover, the higher the losses in the ring waveguide, the higher the required power coupling coefficient κ^2 to achieve critical coupling. Indeed, in our case, a RR near the critical coupling regime is desired, so that changing the GST phase distribution through an optical input pulse is more energy efficient. Therefore, the high finesse approximations (for low ring losses and κ^2) employed in the previous derivation of the RR optical ODE have to be revised.

Another important change introduced by the presence of the PCM cell is that the resonant optical mode in the ring is not symmetric anymore w.r.t. the coupling sections, due to the different effective refractive index of the waveguide segment with GST. We account for this by mathematically treating the two halves of the RR, divided by the coupling regions, separately.

Optics EXPRESS

An introduction to better understand the following arguments can be found in Sections 1 and 2 of the Supplement 1.

With reference to Fig. 4, let us consider the propagation coefficient h_1 corresponding to the right half of the ring:

$$h_1 = A_{\text{scat}} e^{\left(-\alpha_{\text{Si}} - i\frac{\omega}{c} n_{\text{eff}} Si(\omega)\right)(L/2 - L_{\text{GST}}) + \left(-\alpha_{\text{GST}} - i\frac{\omega}{c} n_{\text{eff}} GST(\omega)\right) L_{\text{GST}}}$$

Here, $n_{\text{eff}}Si$ and $n_{\text{eff}}GST$ (α_{Si} and α_{GST}) are respectively the *unperturbed* effective refractive index (attenuation coefficient) of the silicon ring waveguide and of the GST cell, whose length is L_{GST}. A_{scat} is a factor representing the scattering loss of the GST cell. We keep the loss-related part of this expression as it is, while, as in Section 1 of the Supplement 1, we consider a first-order chromatic dispersion relation for the effective refractive indices:

$$\begin{aligned} & e^{-i\frac{\omega}{c} n_{\text{eff}} Si(\omega)(L/2 - L_{\text{GST}}) - i\frac{\omega}{c} n_{\text{eff}} GST(\omega) L_{\text{GST}}} \approx \\ & \approx e^{-i\frac{\omega_r}{c} n_{\text{eff}} Si(\omega_r)(L/2 - L_{\text{GST}}) - i\frac{\omega_r}{c} n_{\text{eff}} GST(\omega_r) L_{\text{GST}}} \cdot e^{-i\frac{\Delta\omega}{c} n_g Si(\omega_r)(L/2 - L_{\text{GST}}) - i\frac{\Delta\omega}{c} n_g GST(\omega_r) L_{\text{GST}}} \approx \\ & \approx e^{-i\frac{\omega_r}{c} n_{\text{eff}} Si(\omega_r)(L/2 - L_{\text{GST}}) - i\frac{\omega_r}{c} n_{\text{eff}} GST(\omega_r) L_{\text{GST}}} e^{-i\frac{L n_g Si(\omega_r)}{2c}\Delta\omega} \equiv \overline{m}_1 e^{-iT_r\Delta\omega/2} \end{aligned} \tag{7}$$

Here, n_gSi, n_gGST are respectively the group index of the silicon ring waveguide and of the GST cell. We neglected the term $\Delta\omega \left(n_g GST(\omega_r) - n_g Si(\omega_r)\right) L_{\text{GST}}/c$ in the exponent, since we assume both $\Delta\omega \ll \omega$ and $L_{\text{GST}} \ll L$ (e.g. $L_{\text{GST}} = 0.5\,\mu\text{m}$ and the ring radius is $R = 15\,\mu\text{m}$). In this case, the linear approximation of the exponential containing $\Delta\omega$ (like in the ring without GST) is not employed, since there are other exponential functions multiplying it. Indeed, it is computationally cheaper to sum all the exponents in a single exponential function. Therefore, we have:

$$h_1 \approx A_{\text{scat}} e^{-\alpha_{\text{Si}}(L/2 - L_{\text{GST}}) - \alpha_{\text{GST}} L_{\text{GST}}} \overline{m}_1 e^{-iT_r\Delta\omega/2} \tag{8}$$

$$h_2 \approx e^{-\alpha_{\text{Si}} L/2} e^{-i\frac{\omega_r}{c} n_{\text{eff}} Si(\omega_r) L/2} e^{-iT_r\Delta\omega} \approx \overline{m}_2 e^{-\alpha_{\text{Si}} L/2 - iT_r\Delta\omega/2} \tag{9}$$

It should be noticed that, because of the loss of symmetry of the optical ring mode w.r.t. the coupling sections, $\overline{m}_1$ and $\overline{m}_2$ can take on a continuous range of complex values of unit modulus, as opposed to $\overline{m}$ (see Section 2 of Supplement 1), which in the case of a normal add-drop RR ideally takes on 1 and -1 only. This happens because the RR resonance condition has changed with the introduction of the GST cell:

$$\omega_r n_{eff} Si(\omega_r)(L - L_{\text{GST}})/c + \omega_r n_{\text{eff}}^{\text{GST}}(\omega_r) L_{\text{GST}}/c = 2\pi m \tag{10}$$

and therefore we have the relation $\overline{m}_1\overline{m}_2 = 1$. Finally, through a similar derivation as for Eq. (S5) in the Supplement 1 but omitting the high finesse approximations, we obtain the optical ODE:

$$\frac{d}{dt}a = \left[\tau_1\tau_2 e^{-\alpha_{\text{Si}}(L - L_{\text{GST}}) - \alpha_{\text{GST}} L_{\text{GST}} - iT_r\Delta\omega} - 1\right]\frac{a}{T_r} + i\frac{\kappa_1}{\sqrt{T_r}} s_{\text{in1}} + i\frac{\kappa_2\tau_1}{\sqrt{T_r}}\overline{m}_2 e^{-\alpha_{\text{Si}} L/2 - iT_r\Delta\omega/2} s_{\text{in2}} \tag{11}$$

Following the structure of Eqs. (S9) and (S10) in the Supplement 1, the outputs are:

$$s_{\text{out1}} = i\kappa_1\tau_2 e^{-\alpha_{\text{Si}}(L - L_{\text{GST}}) - \alpha_{\text{GST}} L_{\text{GST}} - iT_r\Delta\omega}\frac{a}{\sqrt{T_r}} + \tau_1 s_{\text{in1}} - \kappa_1\kappa_2\overline{m}_2 e^{-\alpha_{\text{Si}} L/2 - iT_r\Delta\omega/2} s_{\text{in2}} \tag{12}$$

$$s_{\text{out2}} = i\kappa_2\overline{m}_1 e^{-\alpha_{\text{Si}} L/2 - iT_r\Delta\omega/2}\frac{a}{\sqrt{T_r}} + \tau_2 s_{\text{in2}} \tag{13}$$

To account for silicon nonlinear effects, these equations are solved together with Eqs. (4) and (5), and the following dependencies, discussed in detail in [31,32], are considered: $\Delta\omega = \Delta\omega(\Delta T, N)$ and $\alpha_{Si} = \alpha_{Si}(|a|^2, N)$, similarly as in Eq. (3). Moreover, also the quantities that depend on the

Optics EXPRESS

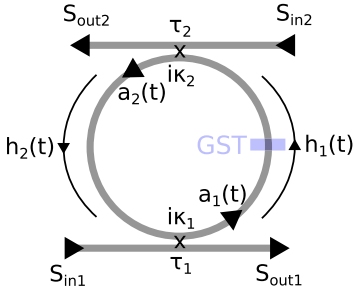

Fig. 4. A schematic of a RR in *add-drop* configuration with GST cell. In this schematic two complex mode amplitudes a_1 and a_2 are considered, located right after coupling Section 1 and 2 respectively.

GST layer state vary with time according to the employed GST model (see Section 2.2). These quantities are $\Delta\omega = \Delta\omega(\Delta T, N, T_{GST}, z_{int})$ and $\alpha_{GST} = \alpha_{GST}(T_{GST}, z_{int})$.

Let us now list and analyse the main differences (which can be considered as corrections) between the naive "uncorrected" optical equations (as employed for the comparison discussed in Section 2.3 and Fig. 3, and based on Eqs. (S6) in the Supplement 1) and the "corrected" optical equations developed in this section:

1. Direct dependency of the *through* port output on the input at the *add* port, provided by the last term in Eq. (12). This term becomes increasingly important as the power loss due to the GST patch on the right arm of the RR grows. Indeed, by contradiction, it can be noticed that without this term there would be no light coming from the ring to the *though* port in the limit case of infinite optical attenuation at the GST cell. Moreover, this term includes a factor $\kappa_1\kappa_2$ and thus, for small coupling coefficient values, it might be negligible w.r.t. the first right hand term in the same equation (related to the light accumulated in the RR), which includes a $\kappa_1\tau_2$ factor instead. However, this is not true anymore if κ_1 is not much smaller than unity and the maximum power accumulated in the ring is not much higher than the input power (i.e., for low *finesse* RRs). E.g., considering $s_{\text{in1}} = 0$, $\kappa_1^2 = \kappa_2^2 = 0.15$ and a ring power enhancement of $|a|^2/(T_r|s_{\text{in2}}|^2) = 3$, the first right hand term in Eq. (12) is only around four times larger than the last right hand term.

2. The two half-ring complex factors h_1 and h_2 are kept separated. Not only does this allow to seamlessly account for the large difference in response due to the azimuthal number parity (e.g., see Fig. 3(b) and 3(c)), but it also allows to model any asymmetry (both in terms of optical loss and phase shift) of the optical paths between the coupling sections, for example due to a PCM cell. Such an asymmetry, for example, accounts for the differences between the steady-state responses shown in Fig. 3 and the corresponding reversed-input plots in Fig. S3 of the Supplement 1.

3. In our model we do not employ $e^{-\alpha L} \approx 1 - \alpha L$, i.e. we do not approximate the exponential accounting for the optical attenuation in the ring waveguide. e.g., setting the power loss of the silicon ring waveguide (without GST cell) to 8dB/cm, the approximation error would be less than 0.004%. However, if we also include the power loss due to a 0.5 µm GST cell in α, then the error increases to around 0.57%, and to around 1.9% for a 1 µm GST cell. Importantly, since this error is made at every time step of the ODEs integration, its effect can accumulate and strongly influence the nonlinear dynamical behaviour of the RR. It should be stressed that, since we need to employ exponential functions anyways to account for the asymmetric phase shift through the RR arms, this approximation would not provide any improvement in computational efficiency.

Optics EXPRESS

4. Our model does not employ the small coupling approximation $\tau = \sqrt{1-\kappa^2} \approx 1 - \kappa^2/2$. E.g., for $\kappa_1^2 = \kappa_2^2 = 0.15$, the approximation error is around 0.33% per coupling section and it doubles for $\kappa_1^2 = \kappa_2^2 = 0.2$. As for the previous point, also this error can accumulate during the ODEs integration and have a strong impact on nonlinear dynamics.

It should be stressed that this model is not meant to accurately describe the involved physical processes. The goal is instead to develop a model that can approximately reproduce experimental data in a certain parameter window (suitable parameter values can be found later on in Sections 2.3 and 3.1, and in Section 4 of the Supplement 1), and that allows to efficiently simulate large circuits of coupled RRs with PCM cells. In particular, our model allows to account for a PCM cell on the ring waveguide, without being constrained by high *finesse* and spatial symmetry requirements.

In our model we do not consider backreflection due to the medium discontinuity at the GST cell borders, since published simulation results show that it is negligible (around -30dB) [37]. Moreover, the most relevant effect that can arise from counterdirectional coupling is resonance-splitting, which usually has a tangible impact only in high-finesse RRs [20]. Indeed, in the literature presenting experimental measurements or simulations of RRs with GST cell there is no evidence or mention of observable resonance splitting [9,14–16,21–26]. In any case, backreflection could be accounted for by simply adding an optical ODE describing the counterpropagating beam in the RR, which would be coupled with the main beam by reflective elements such as the edges of the GST cell.

Equations (11), (12) and (13) were reshaped in order to fit the mathematical structure required by a TCMT Caphe model, namely represented by Eqs. (1) and (2). This allowed to significantly reduce the computational cost of the simulations, and thus the execution speed [29]. A detailed derivation of the final employed equations is reported in Section 3 of the Supplement 1. Finally, if the dynamics of optical time-dependent variables present much faster timescales than their non-optical counterparts, the computational efficiency of the model may be greatly improved by adiabatic elimination [38]. That is, after checking that the error on the dynamics is negligible, the steady-state equations (e.g. see Section 5 in the Supplement 1) can be used instead of the optical ODEs, allowing to employ much larger time steps in the integration of the other ODEs.

3. Simulation results

In this section, we show how the developed RR model with GST cell can be used to obtain crucial insight into the potential improvement of all-optical memory operations, enabled by the optical resonance of RRs. We do so keeping in mind the goal of developing optically tunable weights for neuromorphic computing or photonic plastic synapses, i.e. integrated devices whose transmission is changed in a non-volatile way by a powerful enough optical input. These devices can be used as building blocks for all-optical coherent neural networks whose synaptic weights can adapt to the network input, similarly to what happens in the biological brain.

The employed simulation parameters, if not otherwise specified, are: the same as in Section 2.3 for what regards the optical linear part; those in [31] regarding the nonlinear dynamics of a silicon RR without GST; the parameters presented in Section 4 of the Supplement 1. Moreover, to roughly account for randomness due to experimental noise, white noise was added to the input optical amplitude at each time step, with standard deviation of 3% w.r.t. the input amplitude.

3.1. *Energy efficiency and speed improvement of GST amorphization and recrystallization*

By accounting for silicon nonlinear effects, which shift the RR resonance wavelength during the excitation by pump pulses, our model allows to predict the optimal RR power coupling coefficients (i.e. $\kappa_1^2 = \kappa_2^2$) and wavelength detuning (i.e. the difference between resonance wavelength and

Optics EXPRESS

source wavelength $\Delta\lambda \equiv \lambda_r - \lambda$) that maximizes energy efficiency of memory operations. Such a prediction can provide important qualitative insight, but also quantitative insight once accurate model parameters are experimentally obtained.

We run several simulations with different values of GST cell length, pulse power, RR coupling coefficients and wavelength detuning. In particular, in our parameter sweeps we considered $\kappa_1^2 = 0.01, 0.02, 0.03, \ldots, 0.19, 0.20$ (20 values) and $\Delta\omega = -0.2\,\text{nm}, -0.18\,\text{nm}, -0.16\,\text{nm}, \ldots, 1.8\,\text{nm}, 0.2\,\text{nm}$ (21 values). We found that a favourable GST cell length is 0.7 μm.

Setting the GST cell length to 0.7 μm, the minimum pulse power required to reach the maximum amorphization fraction (≈ 26 mW with 10 ns duration) is achieved for $\kappa_1^2 = 0.13$ and $\Delta\lambda = 0.16\,\text{nm}$ (see Fig. 5(a) for the full parameter sweep results). Clearly, this type of information could not be obtained from simulations that do not account for the relevant nonlinear dynamics. For example, without nonlinear dynamics, the resonant wavelength of the RR would be fixed and therefore we would wrongly obtain that $\Delta\lambda = 0$ optimizes the energy efficiency of memory operations. Furthermore, employing the same optimal parameters and after an exhaustive exploration of different input pulses combinations, we found that full recrystallization (i.e. nullifying the maximum achievable amorphization) could be obtained by inserting four pulses of 10 ns duration: the first of around 23 mW and the others of around 7 mW. The aforementioned input pulses for amorphization and crystallization are shown in Fig. 5(b), and the corresponding temporal evolution of the states in the developed model is represented in Fig. 5(c). In order to obtain access to the steady state values without running the simulation for an unnecessary longer time, we forced the volatile variables back to their initial values after the amorphization and crystallization pulses (artificial cooldown), which has the same effect of waiting until the system reaches its equilibrium again.

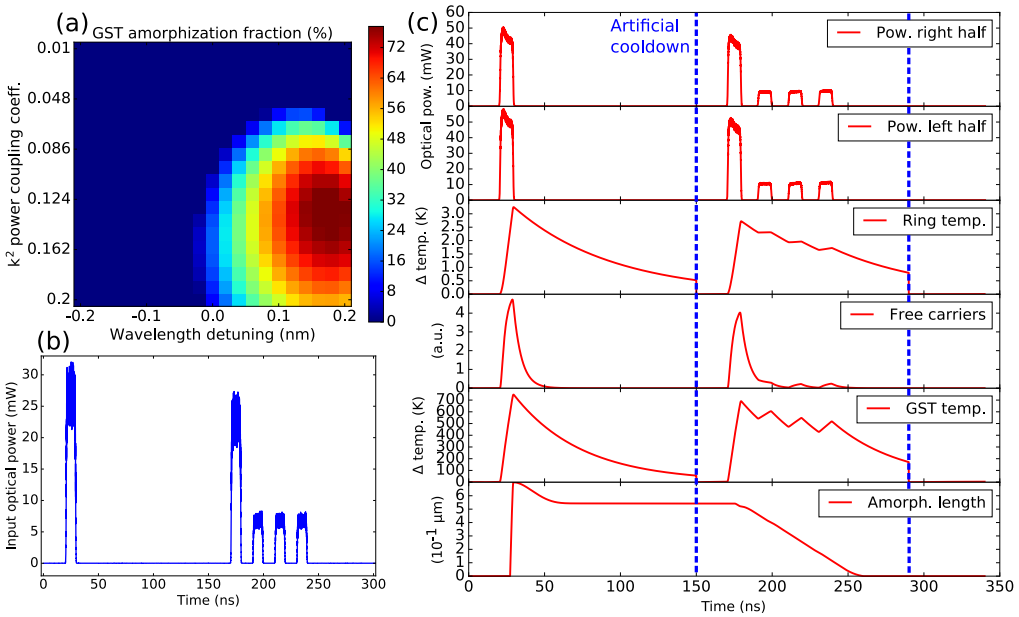

Fig. 5. (a) Colormap of the GST amorphization fraction as a function of resonance wavelength detuning and of the power coupling coefficient. An optical pulse of 10 ns duration and ≈ 26 mW power was considered for amorphization. (b) Inserted pulse sequences for fast and energy efficient amorphization (1^{st} pulse) and subsequent crystallization of the GST cell. (c) Corresponding time evolution of the model states during the insertion of the amorphization and crystallization pulse sequences, in (b).

Optics EXPRESS

Let us now compare the obtained simulation results with the results from the employed GST model (modelling a straight Si waveguide with 4 μm GST cell, validated by fitting the experimental data reported in [19]). With such a comparison, we aim to show, at least qualitatively, the advantages enabled by the RR resonance in terms of speed and energy efficiency of memory operations. To start with, the maximum transmission contrast achieved with our model of a RR with GST is around 15% considering a single input (see Section 3.2 for details). To obtain such a contrast value, we considered an input amorphization pulse of 10 ns conveying only around 0.26 nJ energy, while full recrystallization is achieved within 70 ns with less than 0.5 nJ. In comparison, to achieve a similar contrast considering the basic GST model (based on straight silicon waveguide), a 100ns long amorphization pulse with energy of 1.6 nJ is required (see Fig. S4(a) in the Supplement 1). This shows that, thanks to the RR resonance, both speed and energy efficiancy of memory oprations are substantially improved. Moreover, to obtain the same amorphization length of around 543 nm, the GST on waveguide model requires a pulse more than 50% longer (using the same peak optical power) and it only achieves less than 3% transmission contrast (see Fig. S4(b) in the Supplement 1), compared to around 15% for the RR device case. This result indicates that the optical resonance improves memory operations by reducing the energy required to amoprhize the GST and, at the same time, by enhancing the sensitivity to changes in GST material phase distribution. In addition, the same input pulse that causes the maximum contrast in the case of the simulated RR with GST, is not able to modify the GST crystallinity fraction in the case of its straight waveguide counterpart (see Fig. S4(c) in the Supplement 1). Finally, full recrystallization in the straight waveguide simulation is achieved employing a double-step pulse (as in [19]) 530 ns long and with total energy of more than 3.9 nJ (see Fig. S4(d) in the Supplement 1). Also in this case, the RRs enable a significant improvement in both speed and energy efficiency.

Note that further experimental calibration of the GST model for small cell sizes, which is the subject of future work, would be very beneficial to validate the quantitative accuracy of the above results.

3.2. Reading the memory state: contrast and energy efficiency

The observed large advantage in terms of speed and energy efficiency of memory operations is however relevant only if the memory state can be easily read and used to control subsequent photonic operations. In order to take this aspect into account, in addition to calculating the *transmission relative contrast* (i.e. the difference in transmitted power after and before amorphization, divided by the latter value), we also consider the corresponding *transmission absolute contrast* (i.e. the same difference in transmitted power but divided by the input power), for each output port. The latter provides important information regarding the optical loss of the memory state reading, since it is relative to the total input power.

Moreover, we also monitor the *phase contrast* (i.e. the difference in optical phase of the output after and before amorphization, divided by π), which can be converted into transmission contrast by optical interference. In particular, if the memory device is used as a component of a coherent optical circuit, e.g. as non-volatile weight or as plastic synapse for neuromorphic computing, having a high enough phase contrast can be key, even if the transmission contrast is low. Finally, in order to measure the optical loss corresponding to the obtained phase contrast, we also monitor the *transmission* of each output port after amorphization (given by the fraction of the ouput power w.r.t. the total input power).

We explore how these measures vary in different configurations by performing the aforementioned parameter sweep (coupling coefficients and resonance wavelength detuning), but this time using constant low optical power as input, so as to leave the RR in the linear regime. At first, we considered a single input port (the *in* port) and, considering the two extremes in the achievable crystalline fraction range, we obtained a maximum transmission relative contrast

Optics EXPRESS

of around −15% at the *through* port (Fig. 6(a)), whose absolute value is very similar to the maximum value reported for a straight silicon waveguide with GST in [19]. The *drop* port shows a maximum value of around 21% (Fig. S5(a) in the Supplement 1), with the high contrast area in the parameter space not well overlapping with the *through* port case. But for both output ports, the transmission absolute contrast is always below 3.5% in absolute value (Fig. 6(b) and Fig. S5(b) in the Supplement 1). This indicates that accessing the memory state in the linear regime is quite inefficient in terms of energy. Considering this input configuration, the phase contrast was negligible. Nevertheless, we found that the achievable contrast values can be significantly increased by exploiting the enhanced sensitivity of interference effects in a RR. In particular, by inserting the same constant optical power in both input ports (*in* and *add* ports), we achieved transmission relative contrasts up to 280% at *through* port (Fig. 6(c)) and up to 350% at *drop* port (Fig. S5(c) in the Supplement 1), with the corresponding high contrast areas in the parameter space well overlapping. Still, we notice that the access to the memory state is not energy efficient, being the transmission absolute contrast not higher than 2.5% in absolute value (Fig. 6(d) and Fig. S5(d) in the Supplement 1). Moreover, it should be stressed that when two inputs are considered, very different responses are obtained depending on whether the resonance azimuthal number is even or odd. In this case we considered an even azimuthal number, namely 164. This value is found by setting the resonance wavelength to 1550 nm and the RR radius to about 15 μm.

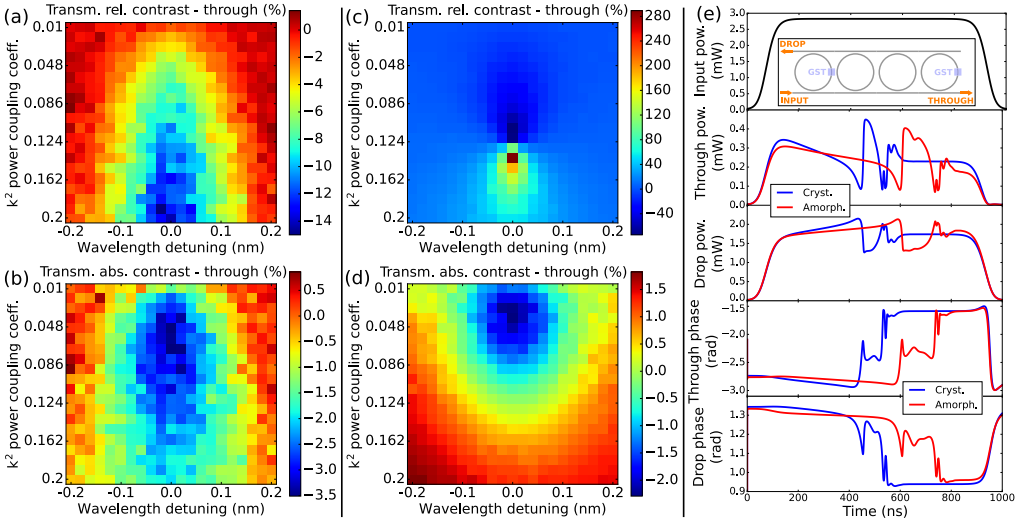

Fig. 6. (a), (b), (c), (d): Colormaps showing the results of the performed parameter sweeps in wavelength detuning and coupling coefficient, at the *through* port of the simulated RR with GST (the counterparts regarding the *drop* port are showed in Fig. S5 in the Supplement 1). (a) and (b): Transmission relative (and absolute, respectively) contrast when a single input port is excited. (c) and (d): The same quantities when both input ports are excited with same power and phase. The considered RR resonance has even azimuthal number. (e): Results of two time-dependent simulations, one for crystalline (red) and the other for amorphized (blue) GST cells, of the silicon photonic circuit schematized in the inset of the top plot. From top to bottom, plots showing input optical power, output power and optical phase at *through* and *drop* ports, as a function of time. To present clear plots in (e), no white noise was added to the input in this case.

Another way to enhance the impact of the GST crystalline fraction on the response of a photonic circuit, is through the excitation of dynamics provided by nonlinear optical cavities. To show this, we employed our model as a building block of a small network of four RRs (Fig. 6(e)),

Optics EXPRESS

two of which with a 0.7 μm GST cell. The execution of the 1 μs simulation (more than 330,000 time steps) required less than 40s on a fairly standard desktop computer (processor: Intel Xeon CPU E5-2650L v3 @ 1.80GHz, 1800 MHz.) employing up to around 0.5 GB of RAM. The two RRs without GST have a relatively small coupling coefficient ($\kappa^2 = 0.04$), so that the power enhancement in the ring waveguide allows to trigger nonlinear effects without reaching input power levels that can change the GST memory state. Considering suitable design parameters ($\kappa^2 = 0.1$ in RRs with GST and an RR interdistance of around half the ring length), we obtained strong contrast in the time-dependent network response, both in terms of output power and optical phase (Fig. 6(e)). Importantly, it should be noticed that this is achieved with relatively low overall power loss. In particular, such an effect is relevant for building plastic recurrent NNs, where the network topology is expanded along the time dimension, and where we believe the potential of the modelled device can be exploited at its fullest.

4. Conclusion

We developed a computationally efficient numerical model for dynamical simulations of silicon ring resonators (RRs) with integrated phase-change material (GST) cells. It accounts for both silicon nonlinear effects (due to free carriers density and temperature increase) and changes in GST material phase distribution due to input optical signals. In particular, we merged a pre-existent compact behavioural model for a waveguide covered by a thin GST film [26] with a dynamical silicon RR model based on time-dependent coupled mode theory. Regarding the latter model, we started from well-known equations for high finesse RRs and we adapted them to account for the non-idealities introduced by the GST film deposited on the ring waveguide, such as asymmetry and high optical absorption. In addition, we restructured the derived equations so to be able to employ them in a commercial circuit simulator (*Luceda Caphe*) that facilitates modularity and to improve computational efficiency of large-scale PIC simulations.

Making use of the developed numerical simulations, we explored different GST cell lengths, optical input pulse powers, RR coupling coefficients and resonant wavelengths. In particular, while achieving the same transmission contrast of 15%, we found that the RR type device offers, in amorphization and recrystallization memory operations respectively, potential switching speed improvements of factors 10 and 7, and energy consumption improvements of factors 6 and 8, as compared to the silicon straight rib waveguide device. Even though for accurate quantitative predictions the model should be fit with more direct experimental data, the obtained results can provide valuable qualitative insight. It should be stressed that, to carry out this kind of numerical investigation correctly, accounting for the dynamic interaction between silicon nonlinear effects and RR resonance (as it is done in the proposed model) is necessary.

In addition, we numerically investigated the contrast in transmission and phase provided by changes in GST phase distribution, for different parameters and configurations. We obtained satisfactory values of transmission contrast in linear regime, although the corresponding energy efficiency is low. However, we observed high power and phase contrast associated with high energy efficiency, in the nonlinear dynamical response of a small silicon RR network. This shows that the considered device is a promising candidate as a building block for plastic photonic recurrent NNs based on silicon nonlinear effects and GST.

It should be stressed that we expect the developed model to easily generalize to other photonic platforms and plastic phase change materials, once the relevant parameters are employed.

As a future development, we aim to fit the developed model with experimental data from direct dynamic measurements of silicon RRs with short GST cells. Then, it will be possible to accurately investigate cascadability of the proposed plastic nodes and their employment in scalable neuromorphic hardware.

Funding. H2020 LEIT Information and Communication Technologies (780848); Fonds Wetenschappelijk Onderzoek (G006020N).

Optics EXPRESS

Acknowledgments. We thank the reviewers for their constructive comments, which have been instrumental in further improving the quality of the paper.

Disclosures. The authors declare no conflicts of interest.

Data availability. Data underlying the results presented in this paper are not publicly available at this time but may be obtained from the authors upon reasonable request.

Supplemental document. See Supplement 1 for supporting content.

References

1. B. J. Shastri, A. N. Tait, T. F. de Lima, W. H. Pernice, H. Bhaskaran, C. D. Wright, and P. R. Prucnal, "Photonics for artificial intelligence and neuromorphic computing," Nat. Photonics **15**(2), 102–114 (2021).
2. C. D. Schuman, T. E. Potok, R. M. Patton, J. D. Birdwell, M. E. Dean, G. S. Rose, and J. S. Plank, "A survey of neuromorphic computing and neural networks in hardware," arXiv preprint arXiv:1705.06963 (2017).
3. D. Marković, A. Mizrahi, D. Querlioz, and J. Grollier, "Physics for neuromorphic computing," Nat. Rev. Phys. **2**(9), 499–510 (2020).
4. D. Christensen, R. Dittmann, B. Linares-Barranco, A. Sebastian, M. Gallo, A. Redaelli, S. Slesazeck, T. Mikolajick, S. Spiga, S. Menzel, I. Valov, G. Milano, C. Ricciardi, S.-J. Liang, F. Miao, M. Lanza, T. Quill, S. Keene, A. Salleo, J. Grollier, D. Marković, A. Mizrahi, P. Yao, J. Yang, G. Indiveri, J. Strachan, S. Datta, E. Vianello, A. Valentian, J. Feldmann, X. Li, W. Pernice, H. Bhaskaran, S. Furber, E. Neftci, F. Scherr, W. Maass, S. Ramaswamy, J. Tapson, P. Panda, Y. Kim, G. Tanaka, S. Thorpe, C. Bartolozzi, T. Cleland, C. Posch, S.-C. Liu, G. Panuccio, M. Mahmud, A. Mazumder, M. Hosseini, T. Mohsenin, E. Donati, S. Tolu, R. Galeazzi, M. Christensen, S. Holm, D. Ielmini, and N. Pryds, "2022 roadmap on neuromorphic computing and engineering," Neuromorphic Comput. Eng. (2022).
5. M. E. Raichle, "The brain's dark energy," Science **314**, 1249–1250 (2006).
6. J. C. Whittington and R. Bogacz, "Theories of error back-propagation in the brain," Trends Cognit. Sci. **23**(3), 235–250 (2019).
7. T. P. Lillicrap, A. Santoro, L. Marris, C. J. Akerman, and G. Hinton, "Backpropagation and the brain," Nat. Rev. Neurosci. **21**(6), 335–346 (2020).
8. A. Taherkhani, A. Belatreche, Y. Li, G. Cosma, L. P. Maguire, and T. M. McGinnity, "A review of learning in biologically plausible spiking neural networks," Neural Networks **122**, 253–272 (2020).
9. C. Ríos, M. Stegmaier, P. Hosseini, D. Wang, T. Scherer, C. D. Wright, H. Bhaskaran, and W. H. Pernice, "Integrated all-photonic non-volatile multi-level memory," Nat. Photonics **9**(11), 725–732 (2015).
10. X. Li, N. Youngblood, C. Ríos, Z. Cheng, C. D. Wright, W. H. Pernice, and H. Bhaskaran, "Fast and reliable storage using a 5 bit, nonvolatile photonic memory cell," Optica **6**(1), 1–6 (2019).
11. J. Feldmann, M. Stegmaier, N. Gruhler, C. Ríos, H. Bhaskaran, C. Wright, and W. Pernice, "Calculating with light using a chip-scale all-optical abacus," Nat. Commun. **8**(1), 1256 (2017).
12. C. Ríos, N. Youngblood, Z. Cheng, M. Le Gallo, W. H. Pernice, C. D. Wright, A. Sebastian, and H. Bhaskaran, "In-memory computing on a photonic platform," Sci. Adv. **5**(2), eaau5759 (2019).
13. Z. Cheng, C. Ríos, W. H. Pernice, C. D. Wright, and H. Bhaskaran, "On-chip photonic synapse," Sci. Adv. **3**(9), e1700160 (2017).
14. I. Chakraborty, G. Saha, A. Sengupta, and K. Roy, "Toward fast neural computing using all-photonic phase change spiking neurons," Sci. Rep. **8**(1), 12980 (2018).
15. J. Feldmann, N. Youngblood, C. D. Wright, H. Bhaskaran, and W. H. Pernice, "All-optical spiking neurosynaptic networks with self-learning capabilities," Nature **569**(7755), 208–214 (2019).
16. I. Chakraborty, G. Saha, and K. Roy, "Photonic in-memory computing primitive for spiking neural networks using phase-change materials," Phys. Rev. Appl. **11**(1), 014063 (2019).
17. J. Feldmann, N. Youngblood, M. Karpov, H. Gehring, X. Li, M. Stappers, M. Le Gallo, X. Fu, A. Lukashchuk, A. S. Raja, J. Liu, C. D. Wright, A. Sebastian, T. J. Kippenberg, W. H. Pernice, and H. Bhaskaran, "Parallel convolutional processing using an integrated photonic tensor core," Nature **589**(7840), 52–58 (2021).
18. S. Raoux, F. Xiong, M. Wuttig, and E. Pop, "Phase change materials and phase change memory," MRS Bull. **39**(8), 703–710 (2014).
19. X. Li, N. Youngblood, Z. Cheng, S. G.-C. Carrillo, E. Gemo, W. H. Pernice, C. D. Wright, and H. Bhaskaran, "Experimental investigation of silicon and silicon nitride platforms for phase-change photonic in-memory computing," Optica **7**(3), 218–225 (2020).
20. W. Bogaerts, P. De Heyn, T. Van Vaerenbergh, K. De Vos, S. Kumar Selvaraja, T. Claes, P. Dumon, P. Bienstman, D. Van Thourhout, and R. Baets, "Silicon microring resonators," Laser & Photonics Rev. **6**(1), 47–73 (2012).
21. W. H. Pernice and H. Bhaskaran, "Photonic non-volatile memories using phase change materials," Appl. Phys. Lett. **101**(17), 171101 (2012).
22. M. Rudé, J. Pello, R. E. Simpson, J. Osmond, G. Roelkens, J. J. van der Tol, and V. Pruneri, "Optical switching at 1.55 μ m in silicon racetrack resonators using phase change materials," Appl. Phys. Lett. **103**(14), 141119 (2013).
23. M. Stegmaier, C. Ríos, H. Bhaskaran, C. D. Wright, and W. H. Pernice, "Nonvolatile all-optical 1× 2 switch for chipscale photonic networks," Adv. Opt. Mater. **5**(1), 1600346 (2017).

Optics EXPRESS

24. J. Zheng, A. Khanolkar, P. Xu, S. Colburn, S. Deshmukh, J. Myers, J. Frantz, E. Pop, J. Hendrickson, J. Doylend, N. Boechler, and A. Majumdar, "Gst-on-silicon hybrid nanophotonic integrated circuits: a non-volatile quasi-continuously reprogrammable platform," Opt. Mater. Express **8**(6), 1551–1561 (2018).
25. S. G.-C. Carrillo, E. Gemo, X. Li, N. Youngblood, A. Katumba, P. Bienstman, W. Pernice, H. Bhaskaran, and C. D. Wright, "Behavioral modeling of integrated phase-change photonic devices for neuromorphic computing applications," APL Mater. **7**(9), 091113 (2019).
26. S. G.-C. Carrillo, A. Lugnan, E. Gemo, P. Bienstman, W. H. Pernice, H. Bhaskaran, and C. D. Wright, "System-level simulation for integrated phase-change photonics," J. Lightwave Technol. **39**(20), 6392–6402 (2021).
27. M. Fiers, T. Van Vaerenbergh, K. Caluwaerts, D. V. Ginste, B. Schrauwen, J. Dambre, and P. Bienstman, "Time-domain and frequency-domain modeling of nonlinear optical components at the circuit-level using a node-based approach," J. Opt. Soc. Am. B **29**(5), 896–900 (2012).
28. A. Yariv, "Coupled-mode theory for guided-wave optics," IEEE J. Quantum Electron. **9**(9), 919–933 (1973).
29. T. Van Vaerenbergh, M. Fiers, J. Dambre, and P. Bienstman, "Efficient simulation of optical nonlinear cavity circuits," Opt. Quantum Electron. **47**(6), 1471–1476 (2015).
30. T. Van Vaerenbergh, "All-optical spiking neurons integrated on a photonic chip," Ph.D. thesis, Ghent University (2014).
31. T. Van Vaerenbergh, M. Fiers, P. Mechet, T. Spuesens, R. Kumar, G. Morthier, B. Schrauwen, J. Dambre, and P. Bienstman, "Cascadable excitability in microrings," Opt. Express **20**(18), 20292–20308 (2012).
32. T. J. Johnson, M. Borselli, and O. Painter, "Self-induced optical modulation of the transmission through a high-q silicon microdisk resonator," Opt. Express **14**(2), 817–831 (2006).
33. M. Mancinelli, M. Borghi, F. Ramiro-Manzano, J. Fedeli, and L. Pavesi, "Chaotic dynamics in coupled resonator sequences," Opt. Express **22**(12), 14505–14516 (2014).
34. M. Borghi, D. Bazzanella, M. Mancinelli, and L. Pavesi, "On the modeling of thermal and free carrier nonlinearities in silicon-on-insulator microring resonators," Opt. Express **29**(3), 4363–4377 (2021).
35. M. Mancinelli, R. Guider, M. Masi, P. Bettotti, M. R. Vanacharla, J.-M. Fedeli, and L. Pavesi, "Optical characterization of a scissor device," Opt. Express **19**(14), 13664–13674 (2011).
36. G. Tanaka, T. Yamane, J. B. Héroux, R. Nakane, N. Kanazawa, S. Takeda, H. Numata, D. Nakano, and A. Hirose, "Recent advances in physical reservoir computing: A review," Neural Networks **115**, 100–123 (2019).
37. C. Rios, M. Stegmaier, Z. Cheng, N. Youngblood, C. D. Wright, W. H. Pernice, and H. Bhaskaran, "Controlled switching of phase-change materials by evanescent-field coupling in integrated photonics," Opt. Mater. Express **8**(9), 2455–2470 (2018).
38. T. Van Vaerenbergh, M. Fiers, J. Dambre, and P. Bienstman, "Simplified description of self-pulsation and excitability by thermal and free-carrier effects in semiconductor microcavities," Phys. Rev. A **86**(6), 063808 (2012).